

Parametric Evaluation of Morphed Wing Effectiveness

*Original*

Parametric Evaluation of Morphed Wing Effectiveness / Servetti, Guido; Cestino, Enrico; Frulla, Giacomo. - In: AEROSPACE. - ISSN 2226-4310. - 13:2(2026), pp. 1-25. [10.3390/aerospace13020187]

*Availability:*

This version is available at: 11583/3007678 since: 2026-02-16T13:07:35Z

*Publisher:*

MDPI

*Published*

DOI:10.3390/aerospace13020187

*Terms of use:*

This article is made available under terms and conditions as specified in the corresponding bibliographic description in the repository

*Publisher copyright*

(Article begins on next page)

Article

# Parametric Evaluation of Morphed Wing Effectiveness

Guido Servetti , Enrico Cestino \*  and Giacomo Frulla 

Department of Mechanical and Aerospace Engineering (DIMEAS), Politecnico di Torino, 10129 Torino, Italy

\* Correspondence: enrico.cestino@polito.it

## Abstract

Recently, continuous improvements in aircraft manoeuvrability and fuel consumption reduction have led researchers to investigate additional wing configurations based on morphing concepts. Morphing is also a potential solution for noise level reduction and may therefore represent an additional benefit. The advantages of morph-type schemes over traditional control surfaces during specific manoeuvres become a key parameter in the preliminary design stage. In this work, three types of airfoil morphing applied to a typical basic wing are considered and analysed: leading-edge morphing, trailing-edge morphing, and rib twist. The aerodynamic performance of each configuration is evaluated through a numerical procedure combining a panel method and a vortex lattice method. Drag reduction in morphed versus conventional wings under identical flight conditions is quantified, allowing the identification of the most efficient configuration. The analyses consider both roll manoeuvres and high-lift flight phases by evaluating changes in design parameters—such as chord-wise hinge positions, span-wise morph distribution, and morphing angles—which are compared and discussed. For the rolling manoeuvre, increasing the span-wise morphing region improves drag reduction, but not by more than 5%. When shifting the hinge position from 60% to 80% of the chord, similar drag reduction levels can be achieved, although the required morph angle differs under the same conditions. The effect of different drag components is also assessed, showing that the induced drag component is predominant for low aspect ratio wings, whereas parasite drag becomes significant at higher aspect ratios. Optimal geometrical configurations are presented and discussed for both manoeuvres. For the rolling, hinge positions yielding typical rolling moment coefficients (i.e.,  $-0.05$ ,  $-0.06$ , and  $-0.08$ ) lie between 65% and 75% of the chord, with span-wise morphing ranges  $40\% < y_{\text{rib}} < 60\%$  producing drag reduction up to 40% compared with a conventional wing. For the high-lift conditions, configurations between  $65\% < x_{\text{hinge}} < 80\%$  and  $50\% < y_{\text{rib}} < 90\%$  allow a drag reduction which can go up to 60%. Another beneficial effect is also observed for the yawing moment coefficient  $C_n$  with a reduction of more than 20% for larger aileron surfaces.



Academic Editor: Christian Breitsamter

Received: 30 December 2025

Revised: 10 February 2026

Accepted: 11 February 2026

Published: 14 February 2026

Copyright: © 2026 by the authors.

Licensee MDPI, Basel, Switzerland.

This article is an open access article distributed under the terms and conditions of the [Creative Commons Attribution \(CC BY\)](https://creativecommons.org/licenses/by/4.0/) license.

**Keywords:** parametric analysis; morph wing; rolling manoeuvre; high-lift flight; preliminary design; low fidelity approach; drag reduction

## 1. Introduction

The morphing wing design concept allows for improved aircraft performance because it enables a greater number of possible wing geometries. The design of an adaptive wing capable of adjusting to flight conditions has remained an open research topic in the aeronautical field for decades [1–5]. Recent reviews have highlighted several aspects of morphing techniques, such as wing shape variations and in-flight structural adaptation [3–5]. In

the state-of-the-art survey presented in [6], typical issues of adaptable structures were discussed, including load transfer from subsystems to the main structure, the trade-off between flexibility and rigidity, scalability and aeroelastic response, and bending–torsion coupling effects. Approaches to these challenges include bi-stable composite materials, auxetic cores, or corrugated structures, particularly for foldable wing-tip mechanisms [7–12]. Corrugated structures enabling increased deformability at the trailing edge are discussed in [7–9], while a fishbone-type polymeric concept for small civil aircraft was manufactured and tested in [10]. Skin deflection associated with highly flexible panels can alter aerodynamic performance, and its relevance must be assessed, as described in [13]. Other structural strategies involve lattice or chiral honeycomb structures capable of responding actively to deformation, which can also contribute to control mechanisms and improve performance [10,11]. Composite materials are also suitable and advantageous for adaptive structures due to their capability to accommodate bending–torsion coupling [14] and their extensive use in aeroelastic tailoring, as shown in [15].

Specific applications have proven feasible in new unmanned aerial vehicle (UAV) designs, enabling improved flight performance and handling qualities. Novel concepts, such as telescopic wings or foldable wings, have been proposed for drone configurations [16–22], some of which are inspired by biological flyers [23]. The Albatross ONE project [2] introduced a free wingtip-swing concept to reduce wing loads and mitigate wingtip stall. Energy saving, emission reduction, and gust-load adaptation have also been demonstrated in morphing wings. Furthermore, the US AFRL and NASA developed an “Adaptive Compliant Trailing Edge” configuration [24], capable of operating up to Mach 0.75 at 40,000 ft by modifying camber and span-wise twist at high actuation rates. The complexity of design, simulation, and control requirements has encouraged researchers to explore alternative solutions, such as span-wise modification, airfoil morphing, wing-surface extension, or sweep-angle variation. One of the most studied methods is airfoil adjustment, where the aerodynamic characteristics of an airfoil are improved by changing chord length, thickness, or camber to increase flight efficiency. Owing to the development of intelligent materials and structures, airfoil adjustment has become increasingly common, achieving better performance than conventional aileron or flap deflections, as described in [24–26]. This technique represents a mesoscale morphing approach. Intelligent and flexible materials were also introduced in the Active Flexible Wing (AFW) and Smart Wing (SW) projects [27] for continuous and seamless wing morphing, enabling structural-weight reductions, increases in flutter critical speed, and improved manoeuvrability. Airfoil-adjustment methods have shown lift-to-drag ratio improvements of up to 51% and maximum lift coefficient increases of 25% through camber variation in the range 0–15% [27,28]. A super-elliptical wing inspired by the varying aspect ratio observed in seagull flight was presented in [29], demonstrating associated lift–drag coefficient improvements.

Morphing requirements [4] aim to improve aerodynamic performance by designing structures capable not only of withstanding prescribed loads but also of adapting their shape. Ideally, no clear distinction should exist between the structure and the actuation system, while flexibility becomes part of the actuation mechanism. This implies a compromise between flexibility and structural-load-carrying capability. A typical morphing concept involves modifying the sectional curvature in the chord-wise direction. Active morphing control can reduce the dynamic response to gust loads in flexible wings, although it may increase structural vibrations [7,30–33]. Handling qualities also play an important role, as evaluated in [31], where only flight performance and handling metrics were considered. The trade-off between structural requirements and aerodynamic efficiency influences aeroelastic behaviour because introducing compliance alters the overall wing response compared with conventional designs. In [30], an aeroelastic assessment using low-fidelity steady

and unsteady aerodynamic models showed conservative estimates for flutter speed in quasi-steady analysis. A rigid wing box with a compliant trailing-edge flap was considered, illustrating the necessary balance between structural rigidity and required compliance for actuation and control. Corrugated structures have also been identified as feasible morphing solutions, particularly for chord-wise curvature variation, although they may increase vibration levels [7].

A structural assessment of a 1:3-scale morphing-flap demonstrator was carried out in [34] with Finite Element and experiments. Additional studies have addressed transitions between subsonic and supersonic regimes, power minimization (in terms of drag), manoeuvrability improvements, and cruise-condition optimisation. Another method for maintaining the desired camber at the trailing edge uses multiple actuators [26]. Actuation remains a critical aspect of morphing-wing design due to its inherent complexity and associated weight. Over the years, numerous mechanisms have been investigated for wing-profile variation [5,35,36], although significant manufacturing challenges persist, particularly for chord-wise and span-wise deformation. Genetic-algorithm optimisation has been used to determine fibre orientations that enhance morphing performance, while topology optimisation has been proposed to achieve optimal trade-offs between stiffness and flexibility [37,38].

Additive-manufacturing approaches have been extensively explored in morphing-wing research, where optimisation plays a central role [39–44], although aerodynamic, structural, and aeroelastic aspects are often addressed separately. Large high-fidelity datasets were used to train deep neural networks for drag minimization and pressure-distribution prediction in the transonic regime, including transition delay effects [39–41]. Genetic-algorithm-based optimisation of fishbone-type morphing structures demonstrated effectiveness at low Reynolds numbers [42,43], while the “FishBAC” concept proved effectiveness across multiple flight conditions [44]. Optimisation strategies have also been integrated into control loops, achieving drag and stress reductions and enabling flutter suppression [32]. Moreover, studies on high-aspect-ratio wings reported significant improvements in roll performance and control robustness compared to conventional ailerons [33].

Three-dimensional effects were analysed in [45] and [46] using a low-fidelity three-dimensional aerodynamic model based on the Prandtl lifting line theory. The study was conducted with both an ideally rigid structure and an increasingly more flexible structure, highlighting the importance of span-wise actuator placement for rib twisting and optimisation. In this case, the actuation involved the entire rib, with maximum drag reduction found for a 40% aileron span length. Parametric studies in [45] demonstrated that higher aspect ratios yield greater drag-reduction benefits.

The design objective of morphing wings remains the identification of the most efficient and cost-effective morphing mode for given mission requirements, with lightweight construction and sufficient load-carrying capability. However, limitations in morphing-aircraft configuration and intelligent-control technologies mean that conventional fixed wings are still preferable in complex operating environments. The increasing design complexity and demanding simulation and control requirements underscore the need for new methodologies to determine suitable morphing schemes and configurations [4].

Building upon the morphing airfoil concepts previously investigated in [45,46], the present paper extends the analysis by systematically assessing the aerodynamic effects of airfoil-morphing strategies for three primary configurations: full rib twist, trailing-edge morphing, and combined leading-edge and trailing-edge morphing [47].

Unlike the prior works, which focused on the development and feasibility of individual morphing concepts, this study provides a unified comparative evaluation of these

configurations under two representative manoeuvring scenarios—(a) rolling manoeuvre and (b) high-lift flight—and benchmarks their performance against classical control surfaces. Aerodynamic performance and improvements are quantified through a parametric preliminary-design procedure.

A novel low-fidelity automated framework combining XFOIL v6.9 (panel method) and AVL v3.40 (vortex-lattice method) is developed to evaluate aerodynamic variations associated with morphing angles, chord-wise hinge locations, and span-wise control-surface lengths. Furthermore, the integration of this parametric framework with optimisation strategies is proposed as a means to accelerate the identification of optimal morphing configurations.

In this paper, the effects of airfoil-morphing strategies are assessed for three primary configurations: full rib twist, trailing-edge morphing, and combined leading-edge and trailing-edge morphing [47]. Two manoeuvring scenarios, representative of symmetric and asymmetric of different aerodynamic conditions, are examined and compared with classical control surfaces: (a) rolling manoeuvre and (b) high-lift flight. Aerodynamic performance and improvements are quantified through a parametric preliminary-design procedure. A low-fidelity automated framework combining XFOIL (panel method) and AVL (vortex-lattice method) is developed to determine aerodynamic variations associated with morph angles, chord-wise hinge locations, and span-wise control-surface lengths. Coupling this parametric framework with optimisation strategies could accelerate the identification of optimal morphing configurations.

## 2. Numerical Procedure and Method

A numerical procedure has been developed to automatically determine the drag reduction in morphing configurations with respect to the conventional aileron for two selected manoeuvres: rolling and high-lift flight. The roll manoeuvre is evaluated by imposing the same rolling moment coefficient and the same lift coefficient for the two compared situations—morphing and conventional—so that a consistent comparison can be performed. All analyses are carried out on a reference “basic wing” representative of a small-medium general aviation aircraft according to a preliminary statistical investigation [48–50]. This reference configuration, summarised in Table 1, consists of a rectangular unswept wing with no dihedral angle and equipped with an LS 0417 airfoil.

**Table 1.** Basic wing geometry.

Parameter	Value
Wing span	10 m
Chord	1.0 m
$\lambda ((2b)^2 / A)$	10
Taper ratio ( $c_t / c_r$ )	1.0
Profile	LS 0417
Constant morph profile position (span-wise)	50%
Trailing edge hinge location (chord-wise)	70%
Leading edge hinge location (chord-wise)	30%
Aileron length (span-wise)	1.5 m
Flap length (span-wise)	6 m

Three different morph types are considered for the two manoeuvring scenarios, defining the selected parameters (such as hinge position, chord-wise and span-wise), defining the configuration, and subsequently calculating the efficacy of the considered manoeuvre. Static analysis is used to compute the rolling moment coefficient assuming rigid-wing

and a stationary, incompressible, viscous flow with Reynolds 2 M (reference wind speed  $v_\infty = 30 \text{ m/s}$ ).

The aerodynamic calculation is divided in two steps: (a) a 2D panel method (XFOIL software [51]) including viscosity models [52], transition criteria of the boundary layer (BL) and separation prediction, used to obtain the airfoil drag component, (b) 3D aerodynamic simulation (AVL Vortex Lattice method [53]) incorporating XFOIL-derived 2D data, used to compute wing-level aerodynamic coefficients. Three morphing types are analysed for the two manoeuvres. The 2D and 3D approaches have been integrated in a single automated procedure, as shown in Figure 1, where the points P1, P2, and P3 are used to define the 2D lift–drag curves [53].

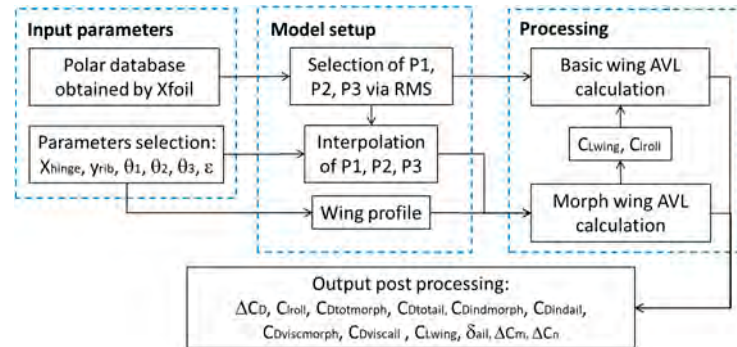


Figure 1. Parametric procedure scheme.

The morph types are described in Figure 2, where the three main categories are identified depending on the movable section: (M1) full rib twist, (M2) trailing-edge morphing, (M3) combined leading-edge and trailing-edge morphing. For the M2 category, three variants can be defined according to Equation (1):

$$\theta_{TE}(x) = \theta_1 + \frac{\theta_2 - \theta_1}{b_{flap}} x_{ail} \tag{1}$$

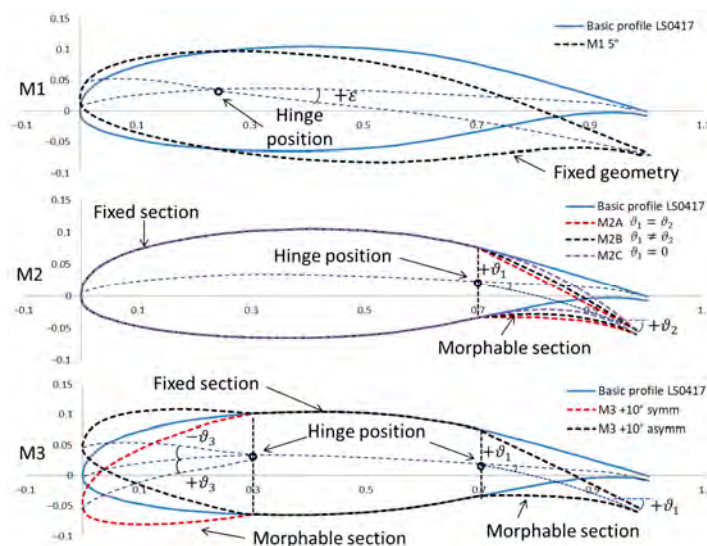


Figure 2. Morph type concepts: M1—rib twist, M2—trailing edge, and M3—trailing edge and leading edge. Typical design parameters definition for morphing analyses.

Here,  $\theta_1$  and  $\theta_2$  are the angles at the hinge position and trailing edge, respectively;  $b_{flap}$  is the length of the flap; and  $x_{ail}$  is the chord-wise coordinate starting from the hinge position to the end of the trailing edge. The morphable sections at the trailing edge and

the leading edge are changing the camber line, maintaining the same distance from the upper and lower surfaces. The morphing angles  $\theta_1$ ,  $\theta_2$ , and  $\theta_3$  are defined by the variation in the camber line from its original position, as indicated in Figure 2.  $\theta_3$  is the angle of deflection at the leading edge. Based on these definitions, five morph configurations can be established as summarised in Table 2.

**Table 2.** Angles definition for each morph type.

Morph Type	$\varepsilon$	$\vartheta_1$	$\vartheta_2$	$\vartheta_3$	$\vartheta_{LE}$	$\vartheta_{TE}$
M1	$\varepsilon$	0	0	0	0	0
M2-A	0	$\vartheta_1$	$\vartheta_2$	0	0	$\vartheta_1 = \vartheta_2$
M2-B	0	$\vartheta_1$	$\vartheta_2$	0	0	$\vartheta_1 + [(\vartheta_2 - \vartheta_1)/b_{flap}] \cdot x_{ail}$
M2-C	0	0	$\vartheta_2$	0	0	$(\vartheta_2/b_{flap}) \cdot x_{ail}$
M3	0	$\vartheta_1$	$\vartheta_1$	$\vartheta_3$	$\vartheta_3$	$\vartheta_1 = \vartheta_2$

The parametric analyses include both 2D parameters (i.e., polar variables  $Re$ ,  $\theta_1$ ,  $\theta_2$ ,  $\theta_3$ , hinge position, and  $x_{hinge}$ ) and 3D parameters, defining different planform geometries with different aileron sizes and positions (i.e.,  $y_{rib}$ ,  $x_{hinge}$ , and angles of morph). For the M3 configuration, the hinge position is fixed at 30% of the chord. The effects of the  $x_{hinge}$  position and the span-wise point  $y_{rib}$  on the drag reduction and rolling moment for various morphing types are investigated through parametric analyses. Optimal configurations, in terms of drag reduction at specific rolling moment coefficients and high-lift flight, are identified.

The 2D airfoil aerodynamic polars, corresponding to specific morph schemes and selected parameters, have been generated using XFOIL and stored in a specific database at different angles of morph and hinge positions. The database is then used to linearly interpolate the aerodynamic values not included within it by MATLAB [54].

Each polar in the database is represented by three selected points, which are required for the 3D evaluation. Accordingly, in AVL, the 2D polars are defined using these three points: P2, corresponding to the minimum drag coefficient (minimum value of  $C_D$ ); P1, corresponding to the lift coefficient ( $C_L$ ) on the left side of the polar (possibly negative); and P3, corresponding to a representative high  $C_L$  on the right side of the polar.

The left branch and the right branch of the polar have been interpolated by a single interpolation function (Figure 3), which is composed of two quadratic functions: one defined by P2 and P1 for the left branch and the other defined by P2 and P3 for the right branch.

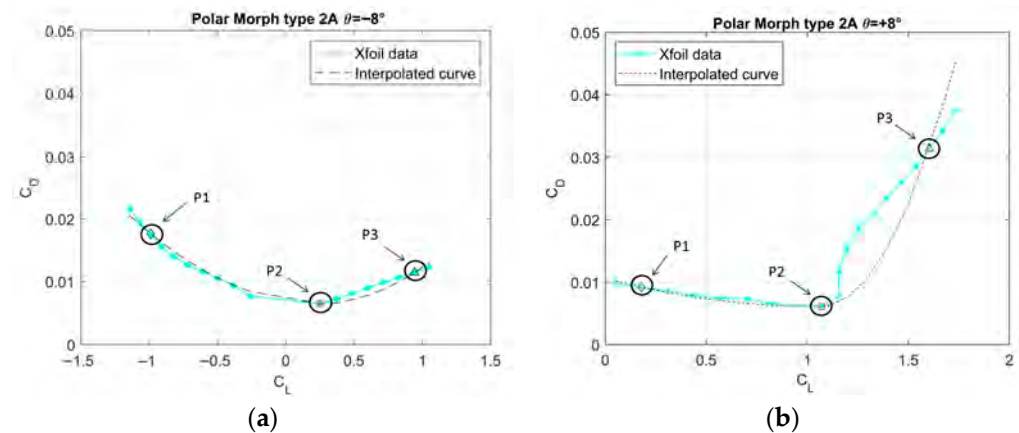


**Figure 3.** Example of P1, P2, P3 selection and polar behaviour with minimum error for a specific configuration: (a) M2A with  $\theta = -8^\circ$ ; (b) M2A with  $\theta = +8^\circ$ .

The identification of the P1 and P3 positions is performed by evaluating the averaged minimum difference with respect to the corresponding XFOIL polar estimation. According to this approach, the variation in the 2D aerodynamics behaviour can be kept within a prescribed tolerance. Table 3 reports the calculated errors for different hinge morphing angles with an example case  $x_{\text{hinge}} = 0.7 c$ , showing that for positive angles, the root mean square (RMS) error is calculated according to the following.

$$RMS\ error = \sqrt{\sum_{i=1}^n \frac{(C_{Dint,i} - C_{Dxfoil,i})^2}{n}} \quad (2)$$

**Table 3.** Example of points obtained by the minimization error procedure for the AVL  $C_D$ - $C_L$  curve definition.

Interpolation Points for M2A ( $x_{\text{hinge}} = 0.7\text{ m}$ )								
	P1		P2 (Min)		P3		RMS Error	
$\theta$ [°]	$C_L$	$C_D$	$C_L$	$C_D$	$C_L$	$C_D$	P1-P2	P2-P3
-10	-1.1049	0.0197	0.0849	0.0065	1.1326	0.0138	$0.30 \times 10^{-3}$	$1.20 \times 10^{-3}$
-8	-0.989	0.0176	0.2489	0.0065	0.9418	0.0114	$0.59 \times 10^{-3}$	$0.77 \times 10^{-3}$
-6	-0.6894	0.0124	0.1747	0.0052	1.091	0.0121	$0.93 \times 10^{-3}$	$0.84 \times 10^{-3}$
0	-0.5863	0.0117	0.2981	0.0052	1.085	0.011	$0.92 \times 10^{-3}$	$0.82 \times 10^{-3}$
6	-0.1129	0.0099	0.9133	0.0057	1.5572	0.0256	$0.30 \times 10^{-3}$	$2.90 \times 10^{-3}$
8	0.1792	0.0092	1.0714	0.0061	1.6028	0.0314	$0.30 \times 10^{-3}$	$6.0 \times 10^{-3}$
10	-0.4265	0.0154	1.224	0.0065	1.7177	0.04	$0.60 \times 10^{-3}$	$11.3 \times 10^{-3}$

It is possible to observe that the errors obtained in the piecewise interpolation differ depending on the region of the interpolated curve. The segment from P1 to P2 exhibits a better correlation with the XFOIL data, whereas the section of the curve between P2 and P3 shows larger deviations, as the transition point introduces an irregular behaviour, also visible in Figure 3b. The maximum error found in the P2–P3 segment is  $11.3 \times 10^{-3}$  at its highest tested morphing angle ( $\theta = +10^\circ$ ), while the maximum error between P1 and P2 is  $0.93 \times 10^{-2}$  at  $\theta = -6^\circ$ . The irregularity is caused by the transition of the boundary layer from laminar to turbulent, as it was also reported in [52].

The 3D simulation of the basic wing, including selected morph scheme, is performed to obtain aerodynamic coefficients such as rolling moment, drag and lift coefficients, yawing moment, and other relevant quantities depending on the manoeuvre considered. Two separate parametric analyses are carried out: one for the rolling manoeuvre and one for the high-lift manoeuvre.

### 2.1. Rolling Manoeuvre Methodology

The comparison of the rolling manoeuvre is carried out between each morphing configuration and the conventional aileron configuration, as shown in Figure 4a and Figure 4b, respectively. The morphing angle along the span-wise direction decreases linearly towards the wing plane of symmetry (x-z plane) for all three morph types. It is defined by the morph angles  $\theta$ ,  $\varepsilon$ , and the span-wise parameter  $y_{rib}$ , which represents the distance between the wing centre and the region where the morphing deflection remains constant (Figure 4b).

The drag coefficient of the entire morphed wing,  $C_{DWing\_morph}$ , and the drag coefficient of the conventional aileron wing,  $C_{DWing\_ail}$ , have been obtained by AVL, and the relative percentage difference is calculated according to the following Equation (3):

$$\Delta C_D = \frac{C_{DWing\_morph} - C_{DWing\_ail}}{C_{DWing\_ail}} \cdot 100 \quad (3)$$

With the conditions reported in Equations (4) and (5), obtained by changing the  $\delta_{ail}$  and  $\alpha$  angles, respectively, to maintain the same rolling moment and lift coefficient, respectively, the following applies:

$$C_{l\_roll\_morph} = C_{l\_roll\_ail} \tag{4}$$

$$C_{LWing\_morph} = C_{LWing\_ail} \tag{5}$$

drag coefficients can be calculated by Equations (6) and (7):

$$C_{DWing\_morph} = f(\theta_1, \theta_2, \theta_3, \varepsilon, x_{hinge}, y_{rib}) \tag{6}$$

$$C_{DWing\_ail} = g(\delta_{ail}, \alpha) \tag{7}$$

It should be noted that the drag coefficient of the morphed wing  $C_{DWing\_morph}$  will depend on the 2D polar variables  $\theta_1, \theta_2, \theta_3, \varepsilon$ , and  $x_{hinge}$ , as well as on the 3D geometric parameter  $y_{rib}$ . In contrast, the drag coefficient of the aileron depends only on the  $\delta_{ail}$  and  $\alpha$ , having the other geometrical parameters fixed.

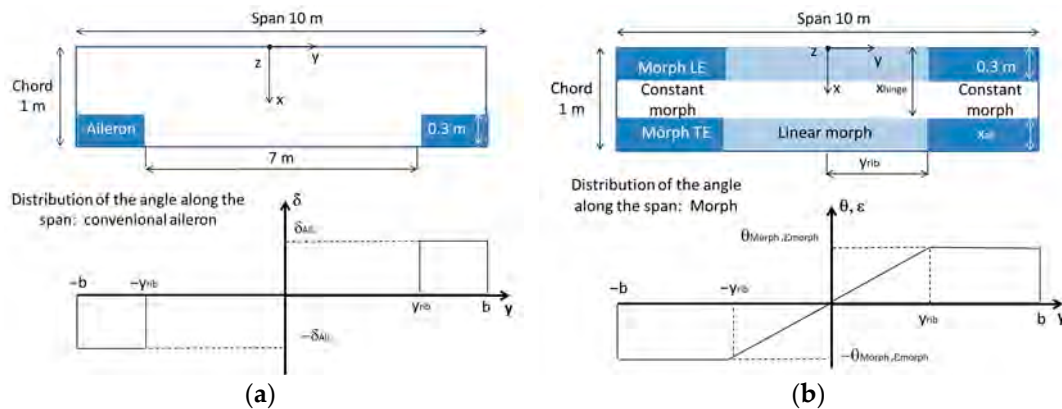


**Figure 4.** Planform wing for the rolling manoeuvre: (a) conventional aileron configuration; (b) morph configuration.

2.2. High Lift Manoeuvre Methodology

In the high-lift flight condition, a flap geometry is considered. The fuselage effect is modelled according to Figure 5a,b. A linear morphing segment is introduced in (Figure 5b), which differs from the conventional flap geometry (Figure 5a). This modification influences the lift distribution near the fuselage, a region which is relevant for the considered manoeuvre.

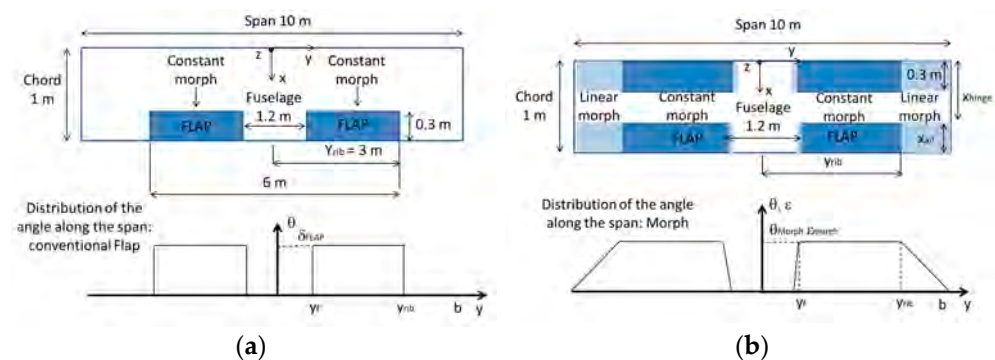


**Figure 5.** Planform configuration and morph angle distribution along the span for the high-lift manoeuvre: (a) conventional aileron configuration; (b) morph aileron configuration.

The morph angle distribution depends on the  $y_{rib}$  and  $y_f$  (with the latter being fixed at  $y_f = 0.6$  m). The definition of the morph type profiles is the same as for the case of the rolling manoeuvre, while the calculation of the drag reduction is different because only the condition of equal lift coefficient is applied. Therefore, it can be written as follows:

$$\Delta C_D = \frac{C_{Dwing\_morph\_HL} - C_{Dwing\_FLAP}}{C_{Dwing\_FLAP}} \cdot 100 \quad (8)$$

with

$$C_{Lwing\_HL\_morph} = C_{Lwing\_HL\_flap} \quad (9)$$

that can be obtained by changing the  $\delta_{FLAP}$ . Hence, the drag coefficient will be represented by the following expressions:

$$C_{Dwing\_morph\_HL} = f(\vartheta_1, \vartheta_2, \vartheta_3, \varepsilon, x_{hinge}, y_{rib}) \quad (10)$$

$$C_{Dwing\_FLAP} = g(\delta_{FLAP}) \quad (11)$$

The calculation of the 2D aerodynamic coefficients  $C_D$  and  $C_L$  follows the same procedure as previously indicated. A difference in the dataset is expected due to the necessity to complete it with a more extended series of polars to include high-lift values. A full turbulent layer can be considered for high angles of attack because the region with high  $C_L$  has a turbulent BL comparable with a full turbulent case. In fact, a full turbulent boundary layer is expected for  $C_L > 1.2$  (Figure 3b).

### 3. Results

A parametric analysis has been carried out for both the rolling manoeuvre and the high-lift flight phase, evaluating several morphing configurations. The chord-wise hinge position  $x_{hinge}$  and the span-wise variable  $y_{rib}$  have been assessed. Each configuration is analysed at different morphing angles, so that each resulting data point—represented as a cloud of points—corresponds to a specific morph type, morphing angle, hinge position, and span-wise location, as summarised in Table 4. In total, 780 morphing configurations for the rolling manoeuvre and 630 for the high lift have been evaluated.

**Table 4.** Parameters of the cloud points analysis for both the rolling manoeuvre and high lift.

Manoeuvre	Morph Type	$\varepsilon, \theta^*$ [°]	$y_{rib}$ [m]	Hinge Position [m]
Rolling	M1, M2A, M2B, M2C,	4, 5, 6,	1.5, 2.0, 2.5,	0.6, 0.65, 0.7,
	M3 Asymm, M3 Symm,	7, 8, 10	3.0, 3.5	0.75, 0.8
High lift	M1, M2A, M2C,	6, 8, 10,	2.5, 3.0, 3.5,	0.6, 0.65, 0.7,
	M3 Asymm, M3 Symm	12, 14, 16	4.0, 4.5	0.75, 0.8

\* Angle of morph for M2B  $\theta_1 = 6^\circ$ ; for other morph types, angles hold the equivalence  $\theta = \theta_1 = \theta_2 = \theta_3$ .

Figure 6 shows the cloud points obtained from the analysis for the rolling manoeuvre. A general trend can be observed: higher rolling moment values correspond to a greater reduction in drag, whereas the span-wise aileron dimension ( $y_{rib}$ ) is less sensitive to variations in drag reduction (Figure 6a).

For the high-lift case, a similar trend can be observed in the sense that higher lift coefficients will have higher drag reduction, but the slope shows a sudden change at about 0.85  $C_L$  (Figure 6b).

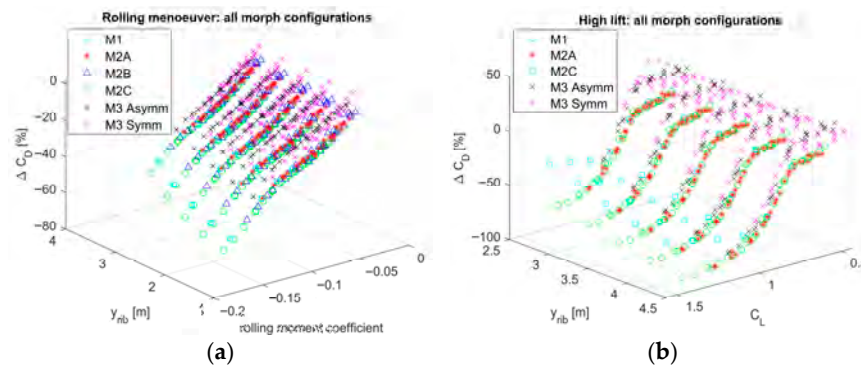


Figure 6. Cloud points for parametric analysis: (a) rolling manoeuvre and (b) high-lift manoeuvre.

3.1. Morph Types Comparison

Drag reduction as a function of the rolling-moment coefficient is presented in Figure 7a for hinge position = 0.6 m and  $y_{rib} = 2.0$  m and in Figure 7c for hinge position = 0.8 m and  $y_{rib} = 3.0$  m. All considered morph types (M1, M2, and M3) are represented and compared. The relationship between rolling-moment coefficient and morphing angle is shown in Figure 7b,d for the same geometrical parameters.

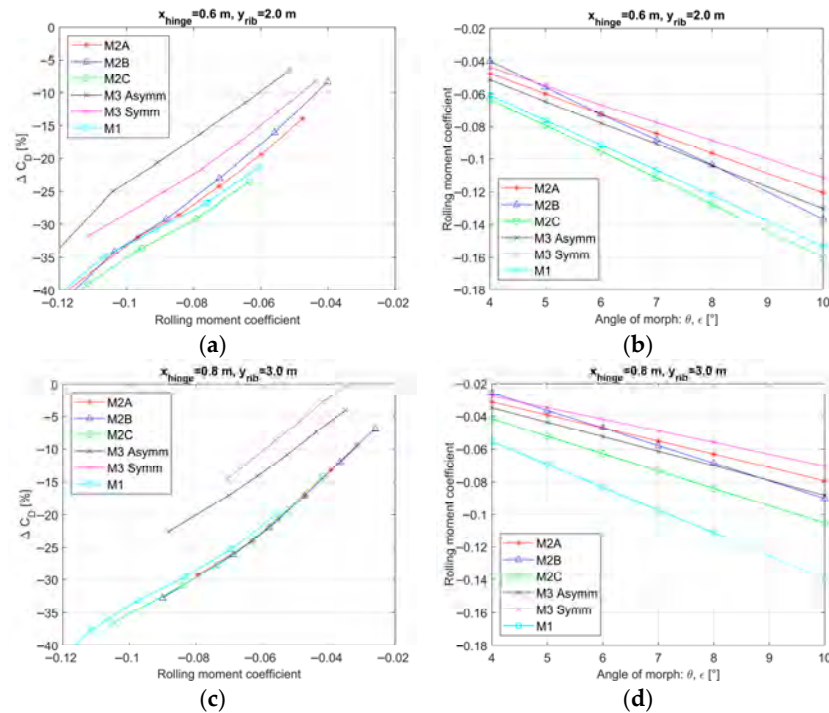


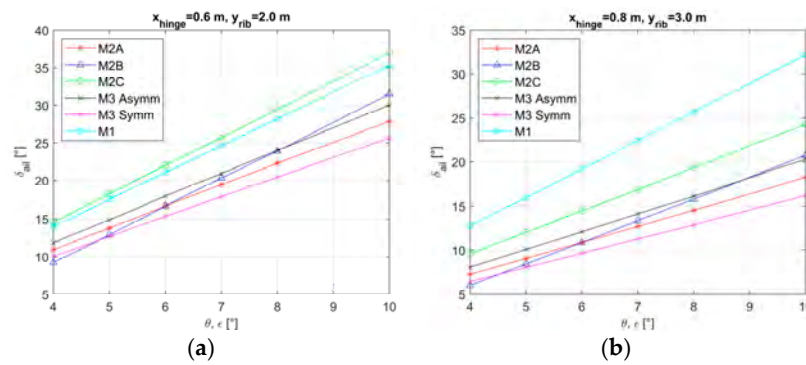
Figure 7. Drag reduction for the rolling manoeuvre at different geometrical parameters: (a)  $\Delta C_D$  reduction vs.  $C_{lroll}$  for larger control surface; (b) morph angle vs.  $C_{lroll}$  for larger control surface; (c)  $\Delta C_D$  vs.  $C_{lroll}$  for smaller control surface; and (d) morph angle vs.  $C_{lroll}$  for smaller control surface.

M2C is the most efficient configuration for hinge position at 0.6 m and  $y_{rib} = 2.0$  m, while for hinge position at 0.8 m,  $y_{rib} = 3.0$  m, all the M2 variants become the most advantageous at a higher rolling moment coefficient, providing similar drag-reduction levels. The observed trend indicates that, for more aft hinge positions and lower  $y_{rib}$ , the M2 configurations achieve a larger drag reduction at equal  $C_{lroll}$  (Figure 7a,c), although the morphing angles required differ (Figure 7b,d).

The M3 configuration is consistently the least effective, exhibiting drag reduction values typically 5–10% lower than those of the M2 variants, depending on the rolling moment coefficient. Figure 7b,d also shows that M2C and M1 produce higher rolling-

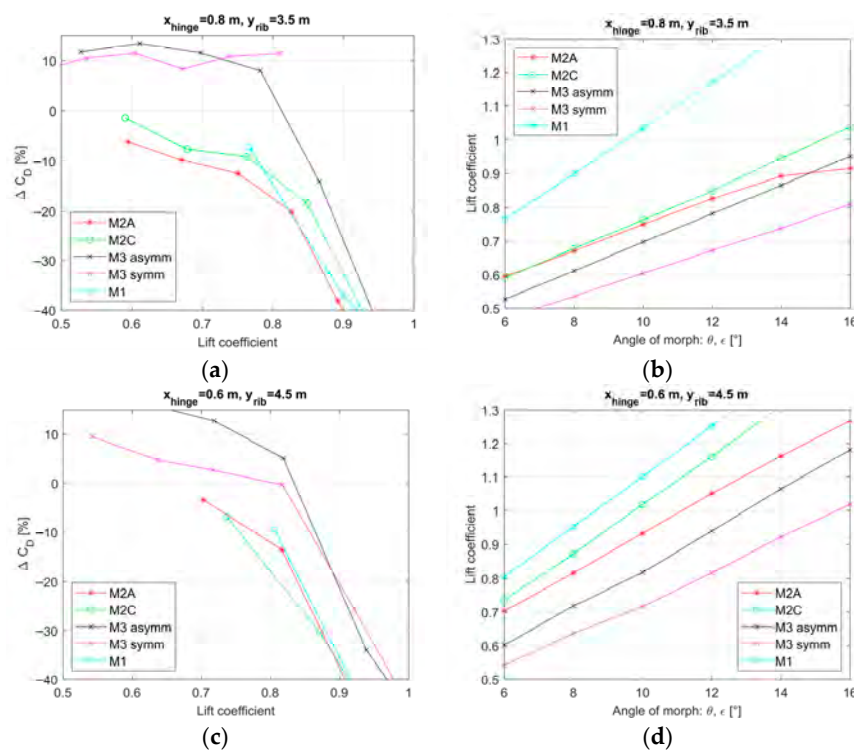
moment coefficients for a given morphing angle. M2C performs better for forward hinge position ( $x_{hinge} = 0.6$  m), whereas for smaller control surfaces ( $x_{hinge} = 0.8$  m), the M1 has the highest rolling moment coefficient.

Figure 8a,b compare the morph types required to generate the same rolling-moment coefficient, highlighting the associated morphing angles for different geometric configurations. As an example, at a morph-angle  $\theta = 6^\circ$ , the same rolling moment coefficient is obtained with a conventional aileron angle  $\delta_{ail} > 16^\circ$  if related to M2A, M2B, and M3, whereas a larger deflection of  $\delta_{ail} > 20^\circ$  is required for M1 and M2C.



**Figure 8.** Aileron angle deflection and angle of morph for the rolling manoeuvre at two geometrical conditions: (a) larger aileron surface; (b) smaller aileron surface.

Drag reduction as a function of the lift coefficient for the high-lift case is reported in Figure 9. Morph types are compared considering two cases:  $x_{hinge} = 0.8$  m with  $y_{rib} = 3.5$  m, and  $x_{hinge} = 0.6$  m with  $y_{rib} = 4.5$  m. Observing Figure 9a,c, M2s and M1 behaviours reveal similar  $\Delta C_D$  with a drag reduction magnitude at  $C_L = 0.75$  between  $-5\%$  and  $-13\%$  for the first case and between  $-5\%$  and  $-10\%$  for the second case.



**Figure 9.** Drag reduction for the high lift at different geometrical parameters: (a)  $\Delta C_D$  reduction vs.  $C_L$  for small control surface; (b)  $C_L$  for small control surface; (c)  $\Delta C_D$  vs.  $C_L$  for larger control surface; and (d)  $C_L$  for larger control surface.

Figure 9b,d show that, for the same morphing angle, the M2C and M1 configurations are the most effective, whereas M2A and M3 yield the lowest lift coefficients. The M1 is particularly advantageous for a smaller flap surface (i.e.,  $x_{hinge} = 0.8$  m;  $y_{rib} = 3.5$  m).

Figure 10 illustrates the effect of the morphing angle at the same lift coefficient for different morph types and geometric parameters. A trend similar to that observed in the rolling manoeuvres is found for the relationship between the conventional flap deflection  $\delta_{FLAP}$  and the respective morphing angle. As an example, M1 and M2C configurations are the most effective as the morphing angle of  $10^\circ$  corresponds to a required conventional-flap deflection of  $\delta_{FLAP} > 20^\circ$ . In contrast, for M2A and M3, the  $\delta_{FLAP}$  is generally  $5^\circ$  lower (Figure 10b).

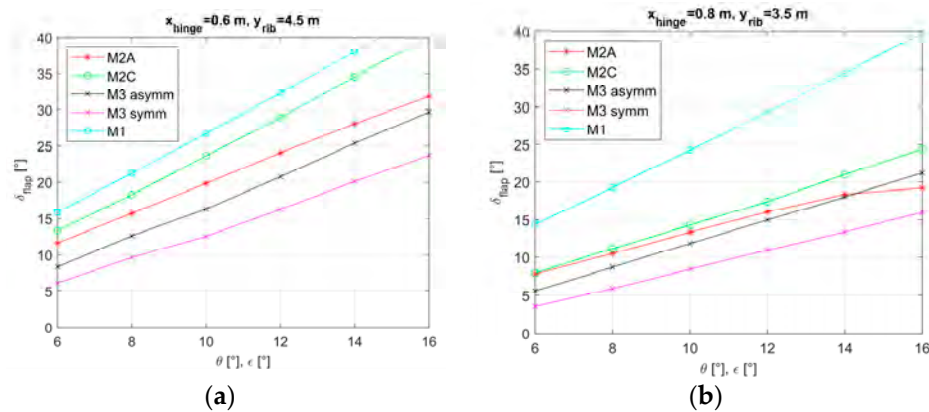


**Figure 10.** Angle of conventional flap and angle of morph for the high lift: (a) smaller flap surface; (b) larger flap surface.

For a more detailed assessment of geometrical parameters, the morph types can be analysed individually, as discussed in the following sections.

### 3.2. Rolling Moment and High Lift Scenarios vs. Geometrical Parameters

The drag reduction obtained for different hinge positions and  $y_{rib}$  values have been analysed for each morphing type (Figures 11–13). For the M2A, M2B, and M2C configurations, higher hinge positions ( $x_{hinge}$ ) generally correspond to greater drag reduction. However, inspection of the individual data points shows that a more forward hinge location (lower  $x_{hinge}$ ) can achieve the same rolling moment coefficient with a smaller morphing angle.

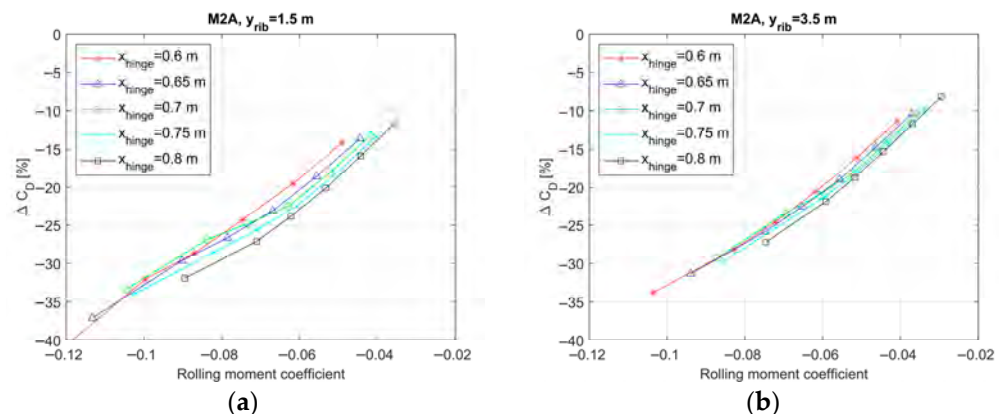


**Figure 11.** Rolling manoeuvre parametric hinge positions results for M2A: (a) Larger aileron surface; (b) Smaller aileron surface.

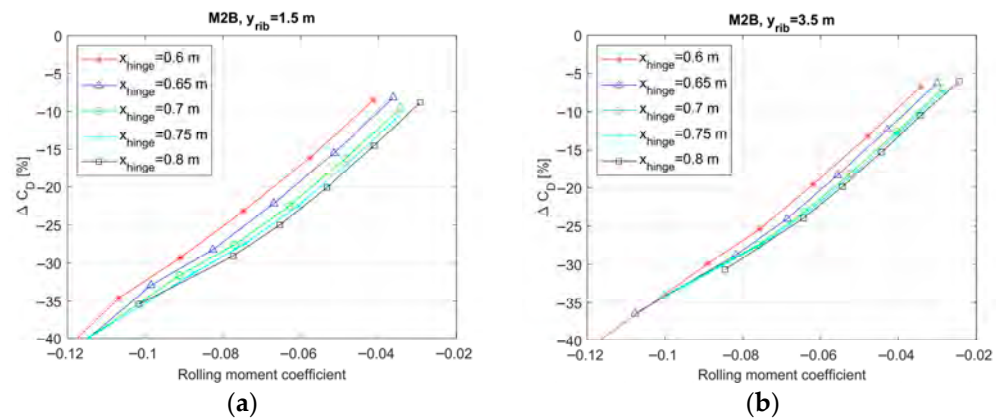


**Figure 12.** Rolling manoeuvre parametric hinge positions results for M2B: (a) Larger aileron surface; (b) Smaller aileron surface.

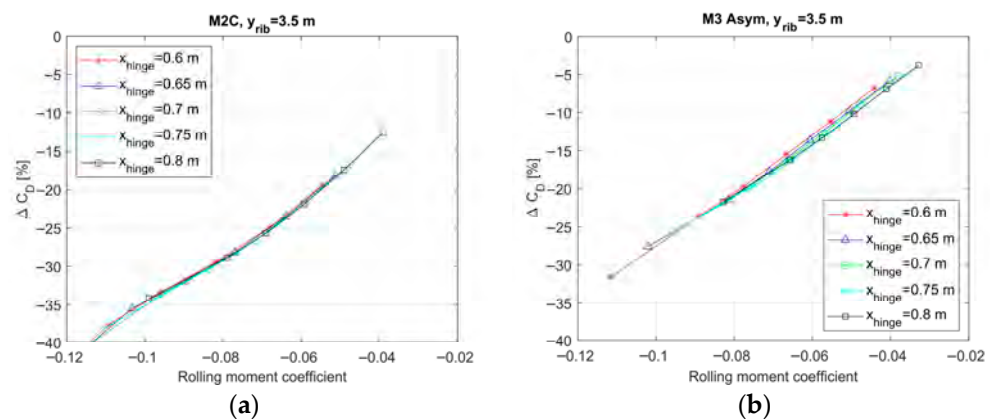


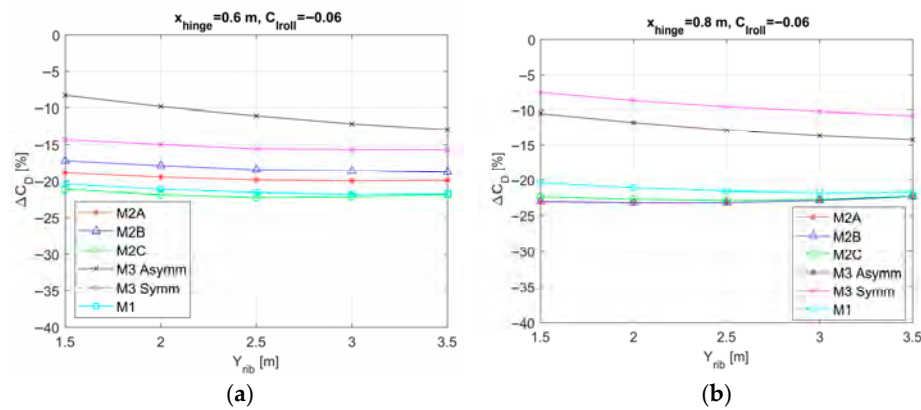
**Figure 13.** Hinge evaluation for two geometrical configurations: (a) M2C; (b) M3 asymmetric.

An opposite trend is observed for the symmetric M3 configuration, while M2C exhibits comparable drag-reduction levels at different hinge positions. With respect to the span-wise parameter  $y_{rib}$ , limited sensitivity is observed for asymmetric M3. In contrast, for M2A, M2B, and symmetric M3, configurations with higher  $y_{rib}$  values (smaller control surfaces; Figures 11b, 12b and 13b) tend to produce similar drag-reduction levels, whereas at lower  $y_{rib}$  values (larger control surfaces; Figures 11a and 12a), the drag-reduction differences between hinge positions become more pronounced, in particular for the M2A and M2B, with the latter being the most sensitive to the hinge position variation. In the case of M2C and asymmetric M3, the hinge variation is almost irrelevant in terms of drag reduction, in particular for the M2C. It is found that for the case of M2C, the influence of  $y_{rib}$  on the drag reduction at  $y_{rib} = 1.5$  m is the most effective case, while for the M2A and M2B, the lower  $y_{rib}$  gives more advantages for most of the cases, but not for all of them. In the case of asymmetric M3, the drag reduction has a small sensitivity on both the  $x_{hinge}$  and  $y_{rib}$  parameters (Figure 13b).

The lower sensitivity of the hinge position for the M2C can be explained by the fact that in this case, the  $\theta_1 = 0^\circ$ , hence the deflection contributing to the lift is towards the end of the trailing edge, so the effective chord-wise length of the flap producing the extra lift is smaller and has a smaller change at different  $x_{hinge}$ . For M2A and M2B, the angle close to the hinge is  $\theta_1 \neq 0$  for M2A and  $\theta_1 = 6^\circ$  for M2B, which shows a higher sensitivity to  $x_{hinge}$ . In these two cases, the effective chord-wise length of the flap starts from the hinge. The low sensitivity of asymmetric M3 to the hinge position can be justified by the similar behaviour to M1, as it was observed in a previous work [47]. The leading edge deflecting in an asymmetric manner with respect to the trailing edge has a comparable

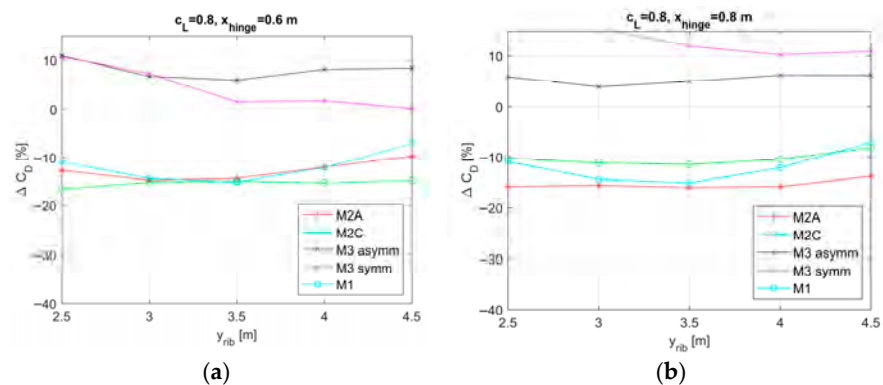
effect of increasing the angle of attack as in the case of M1, in which case the hinge position is not relevant.

Figure 14 illustrates the effect of the  $y_{rib}$  parameter for a fixed  $x_{hinge}$ , evaluated at the same rolling-moment coefficients:  $-0.08$ . A generally flat behaviour is observed across different  $y_{rib}$  values, particularly for the M2 configurations and for M1. However, both morphing types exhibit a shallow minimum around  $y_{rib} = 2.5\text{--}3.0$  m, whereas at  $y_{rib} = 1.5$  m, and the drag reduction is slightly lower, making this the least favourable configuration, even if only by 2–3% (see Figure 14a). The influence of hinge position is more significant: as  $x_{hinge}$  moves aft (e.g.,  $x_{hinge} = 0.8$  m), the curves tend to converge, consistently with the trends observed previously in Figures 11–13. The variation in drag reduction is primarily driven by the rolling-moment coefficient. For example, in the M2A configuration, drag reduction changes from approximately  $-15\%$  at  $C_{lroll} = -0.05$  to  $-25\%$  at  $C_{lroll} = -0.08$ . The M3 configurations show a similar qualitative behaviour, but with greater sensitivity to the geometric parameters, especially in the symmetric M3 case. For asymmetric M3—and for most cases of symmetric M3—the minimum (i.e., optimal) value occurs at  $y_{rib} = 3.5$  m (Figure 14b).



**Figure 14.** Comparison of the morph types at different span parameters for the rolling manoeuvre: (a)  $x_{hinge} = 0.6$  m; (b)  $x_{hinge} = 0.8$  m.

A similar analysis as described above is also done for the high-lift case, as shown in Figure 15, imposing the same lift coefficient at the different  $y_{rib}$  values. In this case, it is more difficult to find a trend for an optimum value of the drag reduction; however, the curve shows a similarity with the rolling manoeuvre because they show a marginal sensitivity to the  $y_{rib}$  for all the morph types (with the exception of symmetric M3), where the change in drag reduction is below 5%. Also in this case, increasing  $y_{rib}$  increases the drag reduction.



**Figure 15.** Comparison of the morph types drag reduction at different span-wise positions and at fixed  $C_{Ls}$  for the high-lift case: (a) hinge position at 0.6 m; (b) hinge position at 0.8 m.

To better understand the geometrical parameters used in the analysis and to identify optimal configurations, the morphing angles are further examined through drag reduction maps as described in the following sections.

### 3.3. Drag Reduction Map

The following parametric maps show a direct relation, at different angles of morphing between the two main parameters defining the hinge position in the span-wise and chord-wise direction:  $x_{hinge}$ ,  $y_{rib}$ , and the resulting drag reduction. The combination of “iso-rolling moment” lines makes it possible to identify the corresponding optimum in terms of drag reduction  $\Delta C_D$  for a particular  $C_{l,roll}$ . It is noteworthy that, at different angles, the gradient of  $\Delta C_D$  remains similar, while only the magnitude of the drag reduction varies. Therefore, a discretization of the morphing angle is sufficient to establish the optimal conditions, since the maps do not change significantly from one angle to another. On the other hand, some relevant differences in the iso-lines are observed among different morphing types.

#### 3.3.1. Rolling Manoeuvre Drag Reduction Maps

Figure 16a shows the drag reduction map for the M2A configuration, where the valley (i.e., region of maximum drag reduction) is located at lower values of  $y_{rib}$  and  $x_{hinge}$ . The gradient of the drag reduction follows the iso- $C_{l,roll}$  lines, indicating that, for a given rolling moment coefficient, it is possible to increase the hinge position value  $x_{hinge}$  and diminish the  $y_{rib}$  while decreasing  $y_{rib}$ , and vice versa. For example, to produce a rolling moment of  $-0.06$  with an angle of morph  $\theta = 6^\circ$ , it is possible to have  $x_{hinge} = 0.75$  m and  $y_{rib} = 1.5$  m, but also  $x_{hinge} = 0.65$  m and  $y_{rib} = 2.9$  m.

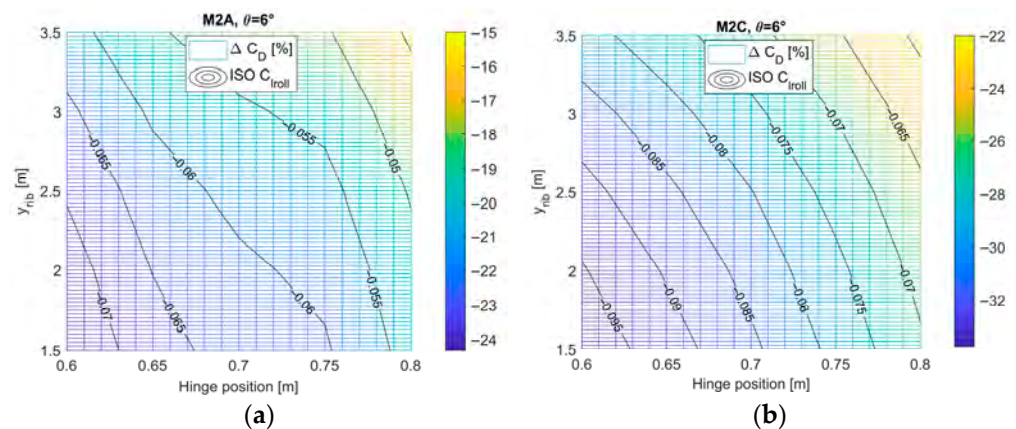


**Figure 16.** Drag reduction maps of the rolling manoeuvre for two different morph cases: (a) M2A at  $\theta = 6^\circ$ ; (b) M2C at  $\theta = 8^\circ$ .

The M2C configuration shown in Figure 16b exhibits a trend similar to that observed for the previously described morphing types; however, at equal morphing angles, both the rolling moment and the drag reduction are increased. Also in this case, the largest drag reduction occurs at lower  $y_{rib}$  and lower  $x_{hinge}$ . Another similarity is that, for a prescribed  $C_{l,roll}$ , different combinations of  $x_{hinge}$  and  $y_{rib}$  can yield the same drag reduction. For example, at a  $C_{l,roll} = -0.08$  with an angle of  $\theta = 6^\circ$ , two equivalent solutions exist at  $x_{hinge} = 0.75$  m with  $y_{rib} = 1.5$  m and  $x_{hinge} = 0.6$  m with  $y_{rib} = 3.2$  m, both providing a similar drag reduction of approximately 28% (Figure 16b).

The drag reduction map for the M3 configuration, shown in Figure 17, exhibits a behaviour different from that of the M2 configurations. In this case, a given iso- $C_{l,roll}$  line can correspond to different levels of drag reduction, depending on the values of  $x_{hinge}$  and  $y_{rib}$ . For instance, at  $C_{l,roll} = -0.085$ , the drag reduction is approximately  $-16\%$  for

$x_{\text{hinge}} = 0.775$  m and  $y_{\text{rib}} = 1.5$  m, whereas it reaches about  $-24\%$  for  $x_{\text{hinge}} = 0.625$  m and  $y_{\text{rib}} = 3.5$  m. In Figure 17a, the comparison of the drag reduction gradient at different  $\theta$  shows that the  $\Delta C_D$  is reducing for higher angles, but the gradient remains unchanged, as it was also found for other morph types.

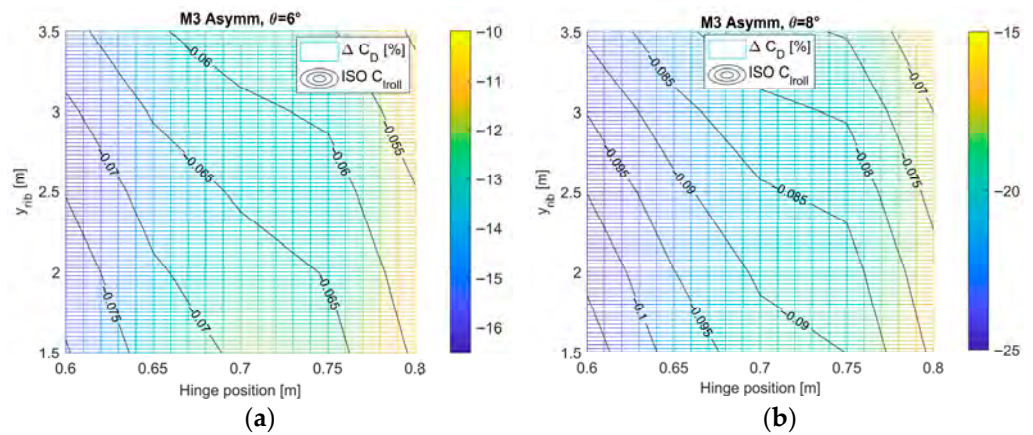


**Figure 17.** Drag reduction maps of the rolling manoeuvre for asymmetric M3: (a)  $\theta = 6^\circ$ ; (b)  $\theta = 8^\circ$ .

Table 5 summarises the results obtained from the parametric maps, highlighting the optimal geometric configurations for generating the required rolling moment. The optimal hinge position is found to lie between 0.65 m and 0.78 m, while the  $y_{\text{rib}}$  can vary between 2.0 m and 3.0 m. In terms of morphing angles, all the types have morph angles with  $6^\circ < \theta < 8^\circ$  for M2A and M2B, while M2C is the one with lower morph angles,  $4^\circ < \theta < 7^\circ$ , and the M3 morph angles are  $4^\circ < \theta < 8^\circ$ . The configurations presented are capable of producing rolling moment coefficients of  $-0.05$ ,  $-0.06$ , and  $-0.08$ , which are representative values for the considered aircraft wing category (Category A [26]).

**Table 5.** Possible optimum configurations for three rolling moment coefficients:  $-0.05$ ,  $-0.06$ ,  $-0.08$ .

Morph Type	$C_{\text{roll}}$	$\theta_1$ [°]	$\theta_2$ [°]	$\theta_3$ [°]	$x_{\text{hinge}}$ [m]	$y_{\text{rib}}$ [m]	$\Delta C_D$ [%]
M2A	$-0.05$	6	6	0	0.78	3.0	$-18$
	$-0.06$	6	6	0	0.65	3.0	$-20$
	$-0.08$	8	8	0	0.68	2.5	$-27$
M2B	$-0.05$	6	6	0	0.78	3.0	$-18$
	$-0.06$	6	6	0	0.68	2.5	$-21$
	$-0.08$	6	8	0	0.72	3.0	$-29$
M2C	$-0.05$	0	4	0	0.73	2.5	$-19$
	$-0.06$	0	5	0	0.76	2.5	$-22$
	$-0.08$	0	7	0	0.70	2.5	$-29$
M3 (Asymm)	$-0.05$	5	5	$-5$	0.77	2.5	$-9$
	$-0.06$	6	6	$-6$	0.78	2.0	$-12$
	$-0.08$	7	7	$-7$	0.65	2.5	$-18$
		8	8	$-8$	0.75	3.0	$-20$

### 3.3.2. High Lift–Drag Reduction Maps

The drag maps for the high-lift configuration follow a concept similar to that used for the rolling manoeuvre, with the difference that iso-lines at a constant lift coefficient  $C_L$  are employed instead of iso-lines of rolling moment coefficient  $C_{\text{roll}}$ .

Figure 18a shows the results for case M2A, where the iso- $C_L$  lines closely follow the gradient of drag reduction. This indicates that, for a given rolling moment coefficient, the drag reduction tends to be similar.

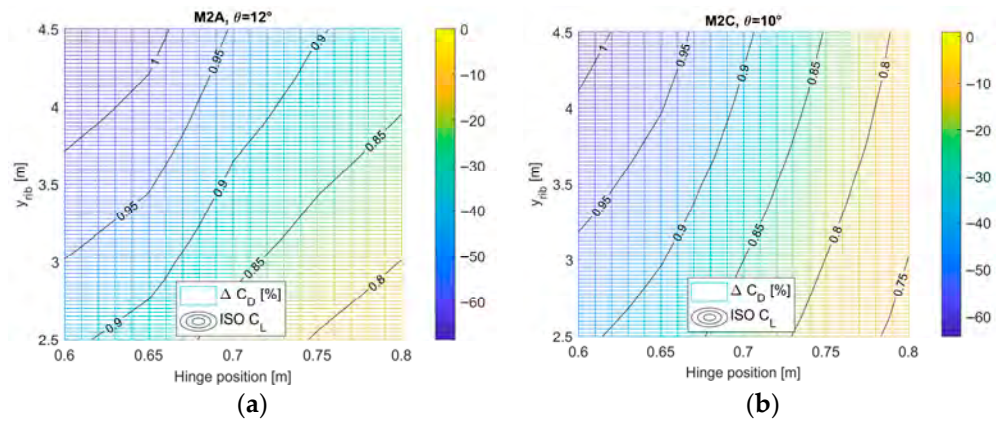


Figure 18. High lift–drag reduction maps for two morph configurations: (a) M2A  $\theta = 12^\circ$ ; (b) M2C  $\theta = 12^\circ$ .

As in the rolling manoeuvre case, the optimal solutions with larger drag reduction are obtained with larger morphing control surfaces, which in this configuration correspond to lower  $x_{hinge}$  value and higher  $y_{rib}$  value. Table 6 provides an example of possible configurations at a selected rolling moment coefficient, showing that different geometries can achieve the same level of drag reduction.

Table 6. Selected optimal configurations M2A.

$C_L$	$\theta_1$ [°]	$\theta_2$ [°]	$\theta_3$ [°]	$x_{hinge}$ [m]	$y_{rib}$ [m]	$\Delta C_D$ [%]
0.8	12	12	0	0.8	3.0	−16
	12	12	0	0.75	2.5	−13
0.9	12	12	0	0.65	2.8	−41
	12	12	0	0.75	4.5	−40
1.0	14	14	0	0.65	2.8	−63
	14	14	0	0.73	4.5	−62

Figure 18b shows that the M2C configuration exhibits a regular behaviour, similar to that observed for the rolling manoeuvre. Also in this case, iso- $C_L$  lines follow the drag reduction gradient. Moreover, these iso-lines tend to be almost vertical, indicating similar  $x_{hinge}$  values. This suggests that improved drag reduction can be found at lower  $x_{hinge}$  values, while the  $y_{rib}$  parameter has a limited influence on drag reduction. Table 7 shows several optimal configurations for the high-lift manoeuvre using the M2C concept. For this morphing type, the morphing angles required to achieve a given lift coefficient are lower compared to those of M2A and M3. For instance, with M2C, a morphing angle of  $\theta = 8^\circ$  yields a drag reduction of 15% at a lift coefficient of 0.8 (Table 7), whereas similar conditions ( $C_L = 0.8, \Delta C_D = -12\%$ ) are obtained with M2A only at higher morphing angles,  $\theta = 12^\circ$  (Table 6).

Table 7. Selected optimal configurations for M2C.

$C_L$	$\theta_1$ [°]	$\theta_2$ [°]	$\theta_3$ [°]	$x_{hinge}$ [m]	$y_{rib}$ [m]	$\Delta C_D$ [%]
0.8	0	8	0	0.65	3.3	−15
	0	8	0	0.69	4.5	−12
0.9	0	10	0	0.65	3.0	−41
	0	10	0	0.7	4.5	−41
1.0	0	10	0	0.67	3.0	−60
	0	12	0	0.72	4.5	−60

The M3 morphing type (asymmetric configuration) exhibits a behaviour that differs from the previously analysed morphing concepts, as the  $y_{rib}$  parameter has a stronger

influence on drag reduction. As shown in Figure 19, varying  $y_{rib}$  at a fixed  $x_{hinge} = 0.6$  m can change the drag variation from an increase of about 10% to a reduction of up to  $-30\%$ . Furthermore, unlike the previous morphing cases, the iso- $C_{L,roll}$  lines do not consistently follow the drag-reduction gradient. Table 8 reports several optimal configurations, indicating that a larger morphing surface is more effective for the high-lift manoeuvre, with optimal ranges of  $0.65 \text{ m} < x_{hinge} < 0.7 \text{ m}$  and  $3.5 \text{ m} < y_{rib} < 4.25 \text{ m}$ .

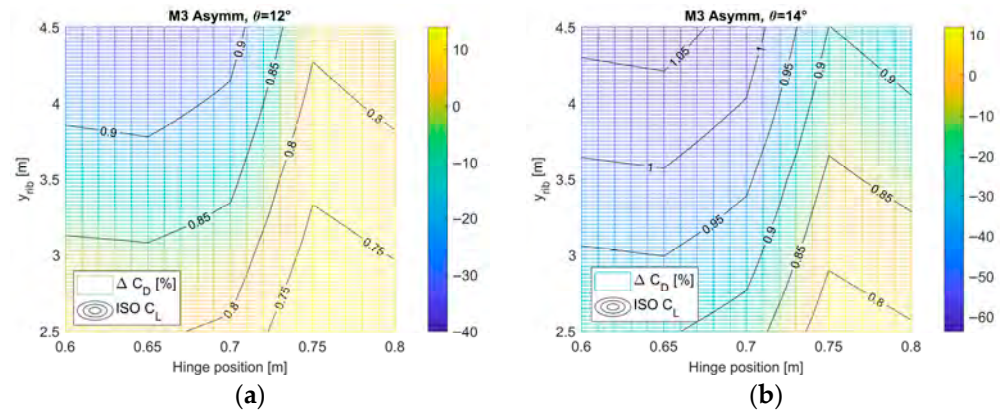


Figure 19. High lift–drag reduction maps for asymmetric M3: (a)  $\theta = 12^\circ$ ; (b)  $\theta = 14^\circ$ .

Table 8. Selected optimal configurations for asymmetric M3.

$C_L$	$\theta_1$ [°]	$\theta_2$ [°]	$\theta_3$ [°]	$x_{hinge}$ [m]	$y_{rib}$ [m]	$\Delta C_D$ [%]
0.8	10	10	−10	0.65	4.0	+8
0.9	12	12	−12	0.65	3.75	−24
	12	12	−12	0.7	4.1	−25
1.0	14	14	−14	0.65	3.5	−52
	12	12	−12	0.7	4.25	−56

From the assessment of all morphing types, a general trend emerges in which larger morphed flap surfaces provide greater aerodynamic benefits. However, several intermediate solutions exist, depending on the morphing concept, for which the same lift coefficient can be achieved using different geometric configurations.

### 3.4. Discussion

The parametric procedure previously presented has been developed to accelerate the preliminary design of a morphing wing by identifying an improved configuration for a selected operating scenario. A linear interpolation approach is employed to estimate the aerodynamic behaviour of the selected configuration using a multi-least root mean squares method. A possible validation of the present results can be carried out by comparison with a previous research activity, as reported in [55]. In the referenced study, a selected configuration was analysed using the same low-fidelity method, but with the inclusion of specific aerodynamic polars. Due to the interpolation process, some differences in the polar values have been introduced in the present procedure, and, therefore, the final estimates may differ slightly in certain cases.

The validity of the calculations in [55] was limited to rolling moment coefficients such that  $C_{L,roll} < |−0.1|$ ; the same limitation applies to the current study.

Another limitation has to be considered when assessing the advantages of the high lift. Because the high lift implies high angles of the control surface, the Xfoil calculation may not be sufficient because of an earlier separation of the flow, and further analysis with high fidelity methods can clarify this aspect.

Some further considerations of the geometrical parameters  $x_{hinge}$  and  $y_{rib}$  on the pitching moment and the yawing moment are noteworthy. Their reduction is defined with the following:

$$\Delta C_m = \frac{C_{m\_morph} - C_{m\_AIL}}{C_{m\_AIL}} \cdot 100 \tag{12}$$

$$\Delta C_n = \frac{C_{n\_morph} - C_{n\_AIL}}{C_{n\_AIL}} \cdot 100 \tag{13}$$

Figure 20a shows that the pitching moment does not change with respect to the conventional aileron case, while Figure 20b indicates a decrease in the yawing moment coefficient, with a reduction ranging from 15% to 23% relative to the baseline wing. This represents a beneficial effect for the rolling manoeuvre, although it becomes less significant for smaller control surfaces (Figure 20b).

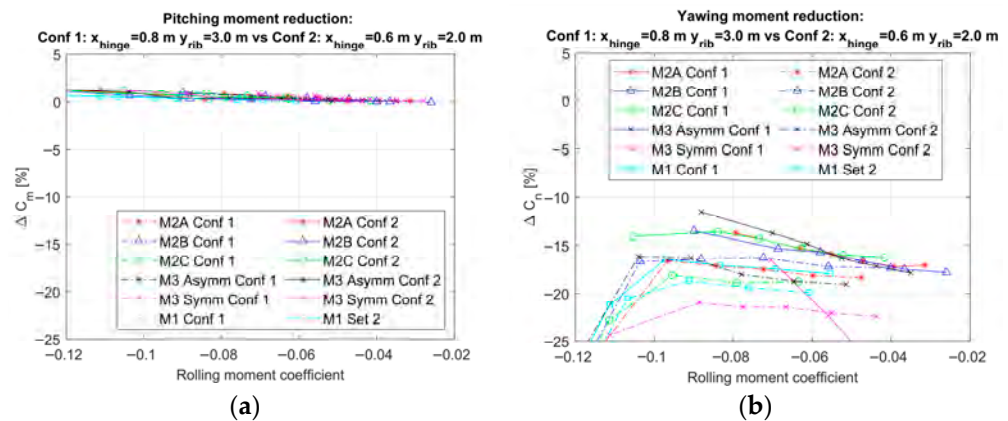


**Figure 20.** Evaluation of the pitching and yawing moment for two different configurations: (a) pitching moment reduction; (b) yawing moment reduction.

Figure 21 presents an assessment of the effect of aspect ratio on the computed drag reduction for the rolling manoeuvre. Different aspect ratios are obtained by increasing the span while maintaining a constant chord and enforcing the condition  $C_L \cdot S = const$ . Hence, the reduction of each drag component is calculated as a percentage of the total drag of the flap (Equations (13) and (14)).

$$\Delta C_{Dv} = \frac{C_{Dv\_morph} - C_{Dv\_FLAP}}{C_{Dtot\_FLAP\_tot}} \cdot 100 \tag{14}$$

$$\Delta C_{Di} = \frac{C_{Di\_morph} - C_{Di\_FLAP}}{C_{Dtot\_FLAP\_tot}} \cdot 100 \tag{15}$$

The induced drag component becomes less significant, circa 2% relative to the total drag reduction as the aspect ratio increases. Conversely, the contribution of viscous drag to the total drag reduction is limited at low aspect ratios but becomes increasingly important for high-aspect-ratio configurations. The induced drag component decreases its relevance with respect to the total drag reduction at high aspect ratios, while the viscous drag component on the total drag reduction is limited for low AR; meanwhile, it tends to be important for high AR configurations.

### 3.5. Future Work

Some of the insights and further advantages that are proposed in the last section can be the incipit for further research. The current approach is based on a static assessment to determine the advantages of the wing morphed concept, but it does not take into account

dynamic behaviour. The yawing moment evaluation can also be part of future work aiming to investigate, in detail, the dynamic effects on the aerodynamic coefficients impacting the flight manoeuvres. Therefore, a more complete model of an aircraft, including other control surfaces, can be used to evaluate the morphing concepts.

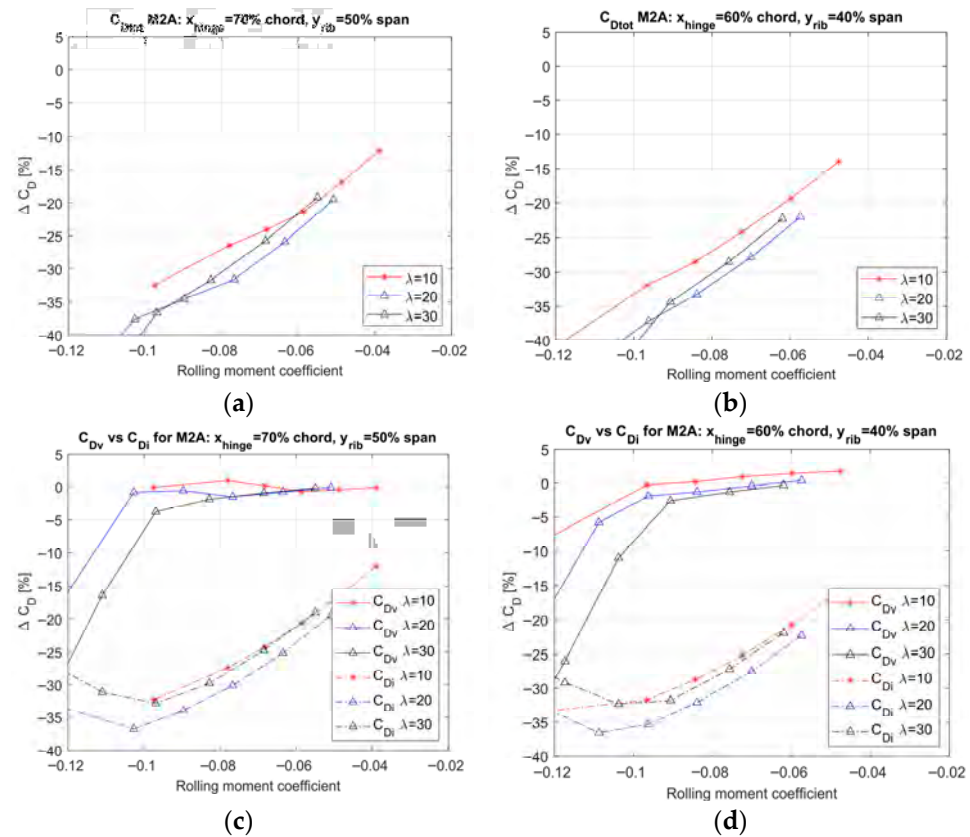


**Figure 21.** Evaluation of the aspect ratio effect on the total drag for the M2A: (a)  $C_{Dtot}$  for  $x_{hinge} = 70\%$  and  $y_{rib} = 50\%$ ; (b)  $C_{Dtot}$  for  $x_{hinge} = 60\%$  and  $y_{rib} = 40\%$ ; (c)  $C_{Dv}$  and  $C_{Di}$  for  $x_{hinge} = 60\%$  and  $y_{rib} = 40\%$ ; (d)  $C_{Dv}$  and  $C_{Di}$  for  $x_{hinge} = 60\%$  and  $y_{rib} = 40\%$ .

Furthermore, the elasticity of the wing, relevant for high aspect ratio wings, can be investigated, including the torsion and bending stiffness.

The two manoeuvres selected showed some limitations at high morphing angle respectively, mainly due to the interpretation of the low fidelity approach at high angles of the control surface. Therefore, a high-fidelity method can be used to better assess the high-lift manoeuvre behaviour, where the current advantage has to be limited at lower  $C_{Ls}$ , reducing the drag advantage estimated.

The proposed preliminary design approach can be used in two ways: either to select a morphing configuration for further detailed analysis, or to be coupled with an optimisation tool to account for additional parameters. In the first case, further aspects can be investigated, such as structural behaviour, morphing mechanism design, and associated added weight, aeroelastic effects, structural integrity, and critical load assessment, which are required to move beyond the preliminary design phase. In the second case, the approach can be extended to include additional parameters—such as Reynolds number, taper ratio, or airfoil profile—by integrating optimisation techniques (e.g., genetic algorithms or design of experiments), thereby managing the increased computational complexity.

## 4. Conclusions

A parametric numerical procedure for identifying optimal morphing-wing configurations at the preliminary design stage has been presented. Three morphing concepts were analysed for rolling manoeuvre and high-lift conditions, considering hinge chordwise position and span-wise control surface length as key design parameters. A low-fidelity aerodynamic approach, based on interpolated lift and drag polars, was adopted under assumptions deemed acceptable for preliminary design.

The results show that larger morphing surfaces generally provide greater drag reduction for both manoeuvres, as higher lift and rolling moment coefficients can be achieved at the same morphing angle. Drag-reduction maps highlight the existence of optimal configurations at fixed morphing angles. For the rolling manoeuvre, optimal solutions were found for  $-0.08 < C_{l,roll} < -0.05$  with  $0.65 \text{ m} < x_{\text{hinge}} < 0.75 \text{ m}$ ,  $2.0 \text{ m} < y_{\text{rib}} < 3.0 \text{ m}$ , and morphing angles between  $5^\circ$  and  $8^\circ$ . For high-lift conditions, optimal ranges were identified for  $0.65 \text{ m} < x_{\text{hinge}} < 0.8 \text{ m}$  and  $2.5 \text{ m} < y_{\text{rib}} < 4.5 \text{ m}$  at  $C_L = 0.8, 0.9$ , and  $1.0$ .

For the rolling manoeuvre, M1 and M2 configurations show similar performance, while M3 generally provides lower drag reduction. M2C is the most effective configuration for larger control surfaces, achieving up to  $\Delta C_D = -30\%$ , whereas M3 asymmetric is more effective for smaller surfaces, showing an opposite trend compared to the other morph types. In high-lift conditions, M1 and M2 remain the most effective, while M3 can be less effective than a conventional aileron at low lift coefficients. A significant increase in drag reduction is observed for  $C_L > 0.8$ , reaching values up to  $-60\%$ , which warrants further investigation using higher-fidelity methods.

Parametric analyses indicate limited sensitivity to  $x_{\text{hinge}}$  and  $y_{\text{rib}}$  for M1 and M2, while M3 configurations show stronger dependence on both parameters. Drag-component analysis confirms that induced drag is the dominant contributor to total drag reduction, although viscous drag becomes increasingly relevant at higher aspect ratios. Other effects related to pitching and yawing moment beneficial variation with respect to the conventional configuration have been pointed out as a starting point for future research activities, as well as structural flexibility. Moreover, the overall scheme of the design can be further exploited with an optimisation tool to evaluate further parameter effects, including structural assessment, dynamic effects, aero-elasticity, mechanism sizing, and weight analysis towards a more detailed phase of design.

The present results are intended to support qualitative and comparative assessments at the preliminary design stage. A comprehensive quantitative validation of the predicted outcomes would require experimental investigations and high-fidelity CFD analyses applied to a real flight aircraft. Despite its limitations, the proposed methodology is suitable for identifying promising morphing-wing configurations.

**Author Contributions:** Conceptualization, E.C., G.F. and G.S.; methodology, E.C., G.F. and G.S.; software, G.S. and E.C.; validation, G.S., G.F. and E.C.; formal analysis, E.C., G.F. and G.S.; investigation, G.S., G.F. and E.C.; resources, G.F. and E.C.; data curation, G.S.; writing—original draft preparation, G.S.; writing—review and editing, G.S., G.F. and E.C.; visualisation, G.S.; supervision, G.F., E.C.; project administration, G.F.; funding acquisition, G.F. All authors have read and agreed to the published version of the manuscript.

**Funding:** This work was possible thanks to the grant released within the Framework Programme for Research and Innovation (2021–2027), grant n° 101159722, with project name “TWINNING FOR EXCELLENCE IN MORPHING AND AEROMECHATRONIC WING CONTROL: A LEAP TOWARDS ECO-SMART AVIATION” acronym (MechaTwing).

**Data Availability Statement:** The data generated in this study are available from the corresponding author upon reasonable request.

**Conflicts of Interest:** The authors declare no conflicts of interest.

## Abbreviations

The following abbreviations are used in this manuscript:

AVL	Athena Vortex Lattice (software name)
BL	Boundary Layer
M1	Morph type 1
M2A	Morph type 2 variant A
M2B	Morph type 2 variant B
M2C	Morph type 2 variant C
M3	Morph type 3
RMS	Root Mean Square
UAV	Unmanned aerial vehicle
HL	High lift manoeuvre
$\lambda$	Aspect ratio
$b$	Semi-wing span
$A$	Wing surface
$c_t$	Chord at the tip
$c_r$	Chord at the root
$\theta_1$	Angle at the hinge position of the morphed trailing edge
$\theta_2$	Angle at the end of the chord of the morphed trailing edge
$\theta_3$	Angle of the leading edge
$\varepsilon$	Angle of the rib twist for morph type M1
$\alpha$	Angle of attack
$\delta_{ail}$	Angle of aileron deflection
$b_{flap}$	Length of the flap
$x_{ail}$	Length of the trailing edge morphable section
$x_{hinge}$	Distance of the hinge position from the trailing edge
$y_{rib}$	Distance defining the morph angle law (linear for rolling, constant step for HL)
$y_f$	Distance defining half of the fuselage diameter
$C_D$	Drag coefficient (generic)
$C_L$	Lift coefficient (generic)
$C_{lroll}$	Rolling moment coefficient
$C_{DWing\_morph}$	Drag coefficient of the morphed wing for the rolling manoeuvre
$C_{DWing\_ail}$	Drag coefficient of the conventional wing for the rolling manoeuvre
$C_{lroll\_morph}$	Rolling moment coefficient of the morphed wing
$C_{lroll\_ail}$	Rolling moment coefficient of the conventional wing
$C_{LWing\_morph}$	Lift coefficient of the morphed wing for the rolling manoeuvre
$C_{LWing\_ail}$	Lift coefficient of the conventional wing for the rolling manoeuvre
$C_{Dwing\_morph\_HL}$	Drag coefficient of the morphed wing for the high-lift manoeuvre
$C_{Dwing\_FLAP}$	Drag coefficient of the conventional wing for the high-lift manoeuvre
$C_{Lwing\_HL\_morph}$	Lift coefficient of the morphed wing for the high-lift manoeuvre
$C_{Lwing\_HL\_flap}$	Lift coefficient of the conventional wing for the high-lift manoeuvre
$\Delta C_D$	Drag reduction (% difference) for rolling and high-lift manoeuvres
$\Delta C_m$	Pitching moment reduction for the rolling manoeuvre
$C_{m\_morph}$	Pitching moment coefficient of the morphed wing
$C_{m\_AIL}$	Pitching moment coefficient of the conventional wing
$\Delta C_n$	Yawing moment reduction
$C_{n\_morph}$	Yawing moment coefficient of the morphed wing
$C_{n\_AIL}$	Yawing moment coefficient of the conventional wing
$\Delta C_{Dv}$	Drag reduction in the viscous term
$C_{Dv\_morph}$	Viscous drag coefficient of the morphed wing

$C_{Dv\_FLAP}$	Viscous drag coefficient of the conventional wing
$C_{Dtot\_FLAP\_tot}$	Total drag coefficient
$\Delta C_{Di}$	Drag reduction in the induced term
$C_{Di\_morph}$	Induced drag coefficient of the morphed wing
$C_{Di\_FLAP}$	Induced drag coefficient of the conventional wing

## References

1. Chu, L.; Li, Q.; Gu, F.; Du, X.; He, Y.; Deng, Y. Design, modeling, and control of morphing aircraft: A review. *Chin. J. Aeronaut.* **2022**, *35*, 220–246. [CrossRef]
2. European Commission. Smarter Wings for Bird-like Flights. Updated 6 December 2020. Available online: <https://ec.europa.eu/research-and-innovation/en/projects/success-stories/all/smarter-wings-bird-flights> (accessed on 6 January 2021).
3. Castillo Acero, M.A.; de la Escalera, F.M.; Essa, Y. Morphed technologies for advanced future commercial aircraft. In *Morphing Wing Technologies*; Elsevier Ltd.: Amsterdam, The Netherlands, 2018; pp. 585–618. [CrossRef]
4. Barbarino, S.; Bilgen, O.; Ajaj, R.M.; Friswell, M.I.; Inman, D.J. A review of morphing aircraft. *J. Intell. Mater. Syst. Struct.* **2011**, *22*, 823–877. [CrossRef]
5. Sofla, A.Y.N.; Meguid, S.A.; Tan, K.T.; Yeo, W.K. Shape morphing of aircraft wing: Status and challenges. *Mater. Des.* **2010**, *31*, 1284–1292. [CrossRef]
6. Ameduri, S.; Concilio, A. Morphing wings review: Aims, challenges and current open issues of a technology. *J. Mech. Eng. Sci.* **2023**, *237*, 4112–4130. [CrossRef]
7. Soneda, K.; Tsushima, N.; Yokozeki, T.; Imamura, T. Aeroservoelastic Characteristics of a Corrugated Morphing Control Surface. *Int. J. Aeronaut. Space Sci.* **2022**, *23*, 723–733. [CrossRef]
8. Kumar, D.; Faruque Ali, S.; Arockiarajan, A. Structural and Aerodynamics Studies on Various Wing Configurations for Morphing. *IFAC PapersOnLine* **2018**, *51*, 498–503. [CrossRef]
9. Gilardelli, A. Soluzioni Strutturali per Ipersostentatori con Caratteristiche Morphing. Master's Thesis, Politecnico di Milano, Milano, Italy, 2015.
10. Li, X.; Sun, L.; Pan, Y.; Guo, X. Honeycomb structure filling morphing wing trailing edge: Design strategy, deformation feedback, and active control. *Program. Mat.* **2024**, *2*, e2. [CrossRef]
11. Wang, Y.; Guo, Y.; Yang, H. Mechanical Properties of Re-Entrant Hybrid Honeycombe Structures for Morphing Wing. *Biomimetics* **2024**, *9*, 521. [CrossRef]
12. Martinez, J.M.; Scopelliti, D.; Bil, C.; Carrese, R.; Marzocca, P.; Cestino, E.; Frulla, G. Design, Analysis and Experimental Testing of a Morphing Wing. In Proceedings of the 25th AIAA/AHS Adaptive Structures Conference, Grapevine, TX, USA, 9–13 January 2017.
13. Kovar, P.; Marhan, T.; Furst, J.; Svacek, P.; Di Cicca, G.; Frulla, G. On determination of Aerodynamic Properties of Morphing Wing by Numerical Simulations. In Proceedings of the ICAST 2025, The 34th International Conference on Adaptive Structure and Technologies, Capua, Italy, 19–21 May 2025.
14. Patuelli, C.; Polla, A.; Cestino, E.; Frulla, G. Experimental and Numerical Dynamic Behavior of Bending-Torsion Coupled Box-Beam. *J. Vib. Eng. Technol.* **2023**, *11*, 3451–3463. [CrossRef]
15. Herencia, J.; Weaver, P.; Friswell, M. Morphing wing design via aeroelastic tailoring. In Proceedings of the 48th AIAA/ASME/ASCE/ASC Structures, Structural Dynamics, and Materials Conference, Honolulu, HI, USA, 23–26 April 2007.
16. Negahban, M.H.; Bashir, M.; Priolet, C.; Botez, R.M. Novel Twist Morphing Aileron and Winglet Design for UAS Control and Performance. *Drones* **2024**, *8*, 392. [CrossRef]
17. Yue, T.; Zhang, X.; Wang, L.; Ai, J. Flight dynamic modeling and control for a telescopic wing morphing aircraft via asymmetric wing morphing. *Aerosp. Sci. Technol.* **2017**, *70*, 328–338. [CrossRef]
18. Ajaj, R.M.; Friswell, M.I.; Dettmer, W.G.; Isikveren, A.T.; Allegri, G. Roll control of MALE UAV using the adaptive torsion wing. *Aeronaut. J.* **2013**, *117*, 299–314. [CrossRef]
19. Liu, Y.; Zhang, J.; Gao, L.; Zhu, Y.; Liu, B.; Zang, X.; Cai, H.; Zhao, J. Employing Wing Morphing to Cooperate Aileron Deflection Improve the Rolling Agility of Drones. *Adv. Intell. Syst.* **2023**, *5*, 2300420. [CrossRef]
20. Ajaj, R.; Friswell, M.; Burchak, M.; Harasani, W. Span morphing using the GNATSpar wing. *Aerosp. Sci. Technol.* **2016**, *53*, 38–46. [CrossRef]
21. Santos, P.D.; Sousa, D.B.; Gamboa, P.V.; Zhao, Y. Effect of design parameters on the mass of a variable-span morphing wing based on finite element structural analysis and optimization. *Aerosp. Sci. Technol.* **2018**, *80*, 587–603. [CrossRef]
22. Ajaj, R.M.; Flores, E.S.; Friswell, M.I.; Allegri, G.; Woods, B.K.S.; Isikveren, A.T.; Dettmer, W.G. The Zigzag wingbox for a span morphing wing. *Aerosp. Sci. Technol.* **2013**, *28*, 364–375. [CrossRef]

23. Hui, Z.; Zhang, Y.; Chen, G. Aerodynamic performance investigation on a morphing unmanned aerial vehicle with bio-inspired discrete wing structures. *Aerosp. Sci. Technol.* **2019**, *95*, 105419. [[CrossRef](#)]
24. Kota, S.; Flick, P.; Collier, F.S. Flight testing of FlexFloil™ adaptive compliant trailing edge. In *Proceedings of the 54th AIAA Aerospace Sciences Meeting, San Diego, CA, USA, 4–8 January 2016*; Export No.: AIAA-2016-0036; AIAA: Reston, VA, USA, 2016.
25. Ameduri, S. Morphing of the leading edge. In *Morphing Wing Technologies*; Elsevier Ltd.: Amsterdam, The Netherlands, 2018; pp. 491–514. [[CrossRef](#)]
26. Arena, M.; Concilio, A.; Pecora, R. Aero-servo-elastic design of a morphing wing trailing edge system for enhanced cruise performance. *Aerosp. Sci. Technol.* **2019**, *86*, 215–235. [[CrossRef](#)]
27. Livne, E.; Weisshaar, T.A. Aeroelasticity of nonconventional airplane configurations—past and future. *J. Aircr.* **2003**, *40*, 1047–1065. [[CrossRef](#)]
28. Osborn, R.; Kota, S.; Ervin, G.; Youngren, H.; Flick, P. Mission adaptive compliant wing: Design, performance and flight test results. In *Proceedings of the 50th AIAA/ASME/ASCE/AHS/ASC Structures, Structural Dynamics, and Materials Conference, Palm Springs, CA, USA, 4–7 May 2009*; American Institute of Aeronautics and Astronautics: Reston, VA, USA, 2009.
29. Bowman, J.; Sanders, B.; Weisshaar, T. Evaluating the impact of morphing technologies on aircraft performance. In *Proceedings of the 43rd AIAA/ASME/ASCE/AHS/ASC Structures, Structural Dynamics, and Materials Conference, Denver, CO, USA, 22–25 April 2002*; p. 1631.
30. Zhang, J.; Shaw, A.D.; Wang, C.; Gu, H.; Amoozgar, M.; Friswell, M.I.; Woods, B.K. Aeroelastic model and analysis of an active camber morphing wing. *Aerosp. Sci. Technol.* **2021**, *111*, 106534. [[CrossRef](#)]
31. Abdulrahim, M.; Lind, R. Flight Testing and Response Characteristics of a Variable Gull-Wing Morphing Aircraft. In *Proceedings of the AIAA Guidance, Navigation, and Control Conference and Exhibit, Providence, RI, USA, 16–19 August 2004*; AIAA: Reston, VA, USA, 2004.
32. Ouyan, Y.; Gu, Y.; Kou, X.; Yang, Z. Active flutter suppression of wing with morphing flap. *Aerosp. Sci. Technol.* **2021**, *110*, 106457. [[CrossRef](#)]
33. Pecora, R.; Amoroso, F.; Lecce, L. Effectiveness of Wing Twist Morphing in Roll Control. *J. Aircr.* **2012**, *49*, 1666–1674. [[CrossRef](#)]
34. Demirci, M.S.S.; Pecora, R.; Chianese, L.; Viscardi, M.; Kaya, M.O. Structural Analysis and Experimental Tests of a Morphing-Flap Scaled Model. *Aerospace* **2024**, *11*, 725. [[CrossRef](#)]
35. Kan, Z.; Li, D.; Shen, T.; Xiang, J.; Zhang, L. Aerodynamic characteristics of morphing wing with flexible leading edge. *Chin. J. Aeronaut.* **2020**, *33*, 2610–2619. [[CrossRef](#)]
36. Monner, H.P.; Bein Th Hanselka, H.; Breitbach, E. Design aspect of adaptive wing—The elastic trailing edge and the local spoiler bump. *Aeronaut. J.* **2000**, *2454*, 15.1–15.9. [[CrossRef](#)]
37. Jensen, P.D.L.; Wang, F.; Dimino, I.; Sigmund, O. Topology Optimization of Large-Scale 3D Morphing Wing Structure. *Actuators* **2021**, *10*, 217. [[CrossRef](#)]
38. Zhu, J.; Yang, J.; Zhang, W.; Gu, X.; Zhou, H. Design and applications of morphing aircraft and their structures. *Front. Mech. Eng.* **2023**, *18*, 34. [[CrossRef](#)]
39. Li, J.; Zhang, M. Data-base approach for wing shape design optimization. *Aerosp. Sci. Technol.* **2021**, *112*, 106639. [[CrossRef](#)]
40. Koreanschi, A.; Gabor, O.S.; Acotto, J.; Brianchon, G.; Portier, G.; Botez, R.M.; Mamou, M.; Mebarki, Y. Optimization and design of an aircraft’s morphing wing-tip demonstrator for drag reduction at low speed, Part I—Aerodynamic optimization using genetic, bee colony and gradient descent algorithms. *Chin. J. Aeronaut.* **2017**, *30*, 149–163. [[CrossRef](#)]
41. Lukić, N.; Ivanov, T.; Svorcan, J.; Simonović, A. Numerical Investigation and Optimization of a Morphing Airfoil Designed for Lower Reynolds Number. *Aerospace* **2024**, *11*, 252. [[CrossRef](#)]
42. Woods, B.K.S.; Friswell, M.I. Preliminary investigation of a Fishbone Active Camber concept. In *Proceedings of the ASME 2012 Conference on Smart Materials, Adaptive Structures and Intelligent Systems, SMASIS 2012, Stone Mountain, GA, USA, 19–21 September 2012*; Volume 2, pp. 555–563. [[CrossRef](#)]
43. Fincham, J.H.S.; Friswell, M.I. Aerodynamic optimization of a camber morphing aerofoil. *Aerosp. Sci. Technol.* **2015**, *43*, 245–255. [[CrossRef](#)]
44. Jia, S.; Zhang, Z.; Dang, Q.; Song, C.; Yang, C. Real-Time Performance Optimization for a Camber Morphing Wing Based on Domain Incremental Model under Concept Drifting. *Aerospace* **2023**, *10*, 853. [[CrossRef](#)]
45. Cestino, E.; Frulla, G.; Lanzillotti, A. Preliminary Assessment of a Warping wing configuration in rolling control. In *Proceedings of the 31st Congress of the International Council of the Aeronautical Sciences, Belo Horizonte, Brazil, 9–14 September 2018*.
46. Frulla, G.; Cestino, E.; Gili, P.; Visone, M.; Scozzola, D. *A Possible Adaptive Wing Apparatus for New UAV Configurations*; SAE Technical Paper 2015-01-2463; SAE: Warrendale, PA, USA, 2015. [[CrossRef](#)]
47. Servetti, G.; Cestino, E.; Frulla, G. Numerical Investigation of different morph wing configurations for the rolling manoeuvre. *J. Intell. Mater. Syst. Struct.* **2025**. *accepted*.
48. Raymer, D. *Aircraft Design a Conceptual Approach*; AIAA Education Series; American Institute of Aeronautics and Astronautics, Inc.: Reston, VA, USA, 2012.

49. Jan, R. Airplane Design part 1. In *Design Analysis and Research Cooperation*; DAR Corporation: Lawrence, KS, USA, 2015.
50. Taylor, J.W.R. *Jane's All The World's Aircraft 1982–1983*; Jane's Yearbooks: London, UK, 1982.
51. Drela, M. XFOIL: An Analysis and Design System for Low Reynolds Number Airfoils. In *Low Reynolds Number Aerodynamics: Proceedings of the Conference Notre Dame, Indiana, USA, 5–7 June 1989*; Springer: Berlin/Heidelberg, Germany, 1989.
52. Drela, M.; Giles, M.B. Viscous-Inviscid Analysis of Transonic and Low Reynolds Number Airfoils. *AIAA J.* **1987**, *25*, 1347–1355. [[CrossRef](#)]
53. Drela, M.; Youngren, H. AVL Overview. 2013. Available online: <http://web.mit.edu/drela/Public/web/avl/> (accessed on 10 September 2015).
54. MathWorks. *MATLAB*, Version R2023a; The MathWorks, Inc.: Natick, MA, USA, 2023. Available online: <https://www.mathworks.com> (accessed on 31 March 2025).
55. Servetti, G.; Cestino, E.; Frulla, G. Investigation of different morph wing configurations for the rolling maneuver. In *Proceedings of the ICAST 2025—The 34th International Conference on Adaptive Structures and Technologies*, Capua, Italy, 19–21 May 2025.

**Disclaimer/Publisher's Note:** The statements, opinions and data contained in all publications are solely those of the individual author(s) and contributor(s) and not of MDPI and/or the editor(s). MDPI and/or the editor(s) disclaim responsibility for any injury to people or property resulting from any ideas, methods, instructions or products referred to in the content.